

Automatic parameter estimation for the Discrete Algebraic Reconstruction Technique (DART)

Wim van Aarle, K. Joost Batenburg and Jan Sijbers

Abstract

Computed Tomography (CT) is a technique for non-invasive imaging of physical objects. In the Discrete Algebraic Reconstruction Technique (DART), prior knowledge about the material's densities is exploited to obtain high quality reconstructed images from a limited number of its projections. In practice, this prior knowledge is typically not readily available. Here, a fully automatic method, called Projection Distance Minimization DART (PDM-DART), is proposed in which the optimal grey level parameters are adaptively estimated during the reconstruction process. Simulation as well as real μ CT experiments show that PDM-DART is capable of computing reconstructed images of which the quality is equally high as that of the reconstructed images computed by conventional DART with exact prior knowledge, thereby eliminating the need for tedious and error-prone user interaction.

Index Terms

computed tomography, segmentation, discrete tomography, automatic parameter optimization, DART, projection distance minimization

Wim van Aarle, K. Joost Batenburg and Jan Sijbers are affiliated with IBBT-Vision Lab, University of Antwerp, Antwerp, Belgium; K. Joost. Batenburg is also affiliated with Centrum Wiskunde & Informatica (CWI), Amsterdam, The Netherlands.

Corresponding author: Wim van Aarle, E-mail: wim.vanaarle@ua.ac.be.

Automatic parameter estimation for the Discrete Algebraic Reconstruction Technique (DART)

I. INTRODUCTION

Discrete tomography algorithms limit the set of possible reconstructions to those that contain only a small number of grey levels. Compared to conventional reconstruction methods (e.g. FBP, SIRT), incorporating this constraint in the reconstruction algorithm results in high quality reconstructions from substantially fewer projection angles, thus reducing the radiation exposure to the scanned sample. In [1], the *Discrete Algebraic Reconstruction Technique (DART)* was introduced. DART is an iterative technique that effectively combines reconstruction and segmentation into a single algorithm. DART exploits prior knowledge about the grey levels of each of the scanned materials to obtain accurate reconstructions even if the amount of projection data is limited (e.g. only a few projection angles are measured, the angular range is limited or the projection data is truncated). DART has already been successfully applied on electron tomography data [2], [3] and to reconstruct three-dimensional grain maps [4].

A key problem when applying DART to experimental datasets is its assumption that the set of grey levels in the unknown reconstructed image is known *a priori*. While this is easy to satisfy in simulation experiments, obtaining such knowledge in practice is non-trivial. Even if the attenuation value of each material is known in advance, accurate hardware calibration is required to translate these values into grey levels for use in the reconstruction. Such a calibration depends on various properties of the scanning system, which are typically not available to the user. Furthermore, calibration parameters may change over time. In X-ray transmission tomography, for example, the X-ray source constantly heats up during scanning, changing the spectrum of the emitted X-rays. While this may have a negligible effect during a single scan, batch processing of scans is rendered impossible.

The knowledge of the reconstruction's grey levels is of crucial importance to obtain high quality DART reconstructions. In Fig. 1, DART reconstructions are shown of a binary phantom image. Each reconstruction was performed adopting a different grey level for the foreground, ρ . Clearly, only with a correct estimation of ρ a sufficiently accurate reconstruction can be achieved. Note that the estimation of the threshold value, τ , used in the segmentation phase of each DART iteration, also influences the reconstruction accuracy. The combination of grey levels and threshold values will be referred to as the *segmentation parameters of DART*.

To estimate the grey levels of an image composed of only a few grey levels, the semi-automatic *Discrete Grey Level Selection (DGLS)* method was introduced in [5] (Fig. 2b). For each grey level, the user selects an area in the reconstruction volume that is assumed to be homogeneous. These user-selected parts are set to a candidate grey level, after which their forward projection is subtracted from the measured projection data. The optimal grey

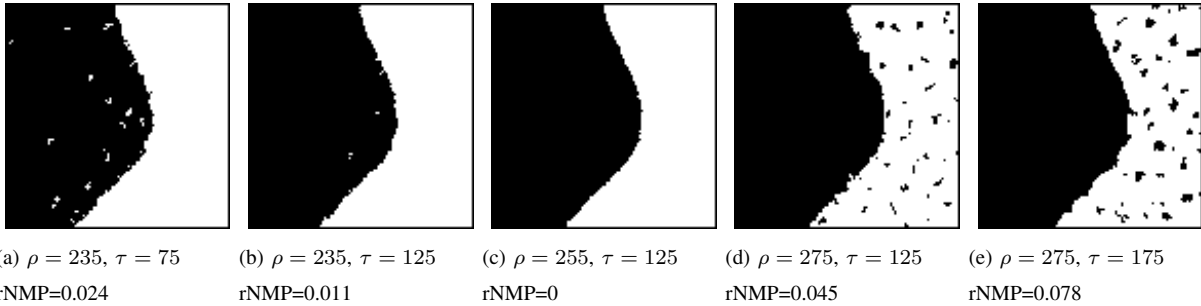


Fig. 1. Parts of DART reconstructions of Fig. 3a for different values of ρ and τ (with 30 equiangular projections). For each (ρ, τ) combination, the relative Number of Misclassified Pixels (rNMP) is given. The rNMP is defined by the number of erroneously classified pixels divided by the amount of non-zero pixels in the phantom image.

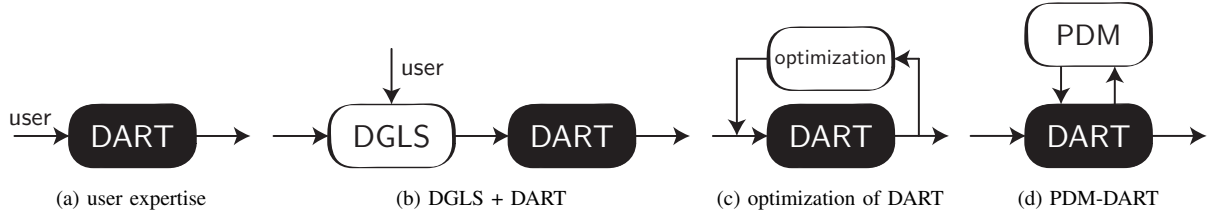


Fig. 2. Schematic overview of various methods to estimate the segmentation parameters of DART. (a) *User expertise* is used to set the correct parameters. (b) The DGLS method is used *prior* to DART to semi-automatically estimate the correct grey levels. (c) An optimization strategy is used to automatically minimize the projection difference between the DART reconstructed images and the measured projection data. (d) The PDM segmentation strategy is used *within* each DART iteration to automatically estimate the optimal grey levels and threshold values.

levels are those for which this residual sinogram is the least inconsistent. With DGLS, the optimal threshold values can not be estimated and still have to be set manually. Furthermore, it is not always possible to manually select a homogeneous region. For example, in bone or foam-like objects, there are no sufficiently large homogeneous areas.

In [6], the projection difference was proposed as a cost function to optimize the segmentation parameters of DART. Optimization strategies, such as the Nelder-Mead simplex search [7] or the more advanced adaptive surrogate modelling optimization [8], can then be employed to obtain accurate values (Fig. 2c). Since such an estimation approach requires a full DART reconstruction for each function evaluation in the optimization process, it is computationally very inefficient.

In this work, the DART method is extended with an advanced segmentation algorithm. In the original DART description [1], intermediate reconstructions are segmented using a global thresholding approach with fixed, a priori specified, segmentation parameters. Here, a more advanced segmentation called Projection Distance Minimization (PDM) [9] is applied in each iteration of DART. This method is hereafter referred to as *PDM-DART*. In *PDM-DART*, the threshold values and grey levels are automatically optimised such that the Euclidean distance between the projection of the intermediate segmented image and the measured projection data is minimal. By applying PDM-DART results are obtained that are comparable to those obtained by conventional DART, without prior knowledge

about the segmentation parameters. This eliminates the need for labour intensive user interaction.

This paper is structured as follows. In Section II, notation for iterative and discrete tomography is presented. Section III then gives a detailed description of PDM-DART. In the subsequent Section IV, the proposed method is experimentally validated on simulated as well as experimental data. These results are discussed in Section V. Finally, in Section VI, conclusions are drawn.

II. NOTATION

Let $\mathbf{v} = (v_j) \in \mathbb{R}^n$ denote the discretised square image of an object, with n the number of pixels. It is assumed that the object is completely contained within this square.

In a parallel beam projection geometry, projection data is measured along lines $l_{\theta,t} = \{(x,y) \in \mathbb{R} \times \mathbb{R} : x \cos \theta + y \sin \theta = t\}$, where $\theta \in [0, \pi)$ represents the angle between the line and the y -axis and t represents the coordinate along the projection axis. In practice, a projection is measured at a finite set of projection angles and at a finite set of detector cells, each measuring the integral of the object density along a ray. Let $\mathbf{p} = (p_i) \in \mathbb{R}^m$ denote the measured projection data, with m the total number of detector cells times the number of projection angles.

The Radon transform of the object for a finite set of projection directions can be modelled as a linear operator \mathbf{W} , called the *projection operator*, which maps the image \mathbf{v} to the projection data \mathbf{q} :

$$\mathbf{q} := \mathbf{W}\mathbf{v}. \quad (1)$$

In Eq.(1), $\mathbf{W} = (w_{ij})$ is an $m \times n$ matrix where w_{ij} represents the contribution of image pixel j to detector value i . The vector \mathbf{q} is called the *forward projection* or *sinogram* of \mathbf{v} .

The tomographic reconstruction problem can be modelled by the recovery of \mathbf{v} from a given vector of projection data \mathbf{p} by solving the following system of equations:

$$\mathbf{W}\mathbf{v} = \mathbf{p}. \quad (2)$$

In the remainder of this work, the *Simultaneous Iterative Reconstruction Technique (SIRT)*, as described in [10], will be used to solve Eq.(2). SIRT is an iterative algorithm that finds a solution $\tilde{\mathbf{v}}$ such that the weighted squared projection difference $\|\mathbf{W}\tilde{\mathbf{v}} - \mathbf{p}\|_R = (\mathbf{W}\tilde{\mathbf{v}} - \mathbf{p})^T \mathbf{R}(\mathbf{W}\tilde{\mathbf{v}} - \mathbf{p})$ is minimal. $\mathbf{R} \in \mathbb{R}^{m \times m}$ is a diagonal matrix that contains the inverse row sums of \mathbf{W} : $r_{ii} = 1 / \sum_j w_{ij}$. The update step of SIRT is given by:

$$v_j^{(k+1)} = v_j^{(k)} + \lambda \frac{1}{\sum_{i=1}^m w_{ij}} \sum_{i=1}^m \frac{w_{ij} (p_i - \sum_{h=1}^n w_{ih} v_h^{(k)})}{\sum_{h=1}^n w_{ih}}. \quad (3)$$

In Eq.(3), λ is a relaxation parameter.

For the case $\bar{\mathbf{v}}^{(0)} = \mathbf{0}$, the SIRT algorithm is a *linear* algorithm in the sense that a reconstructed image $\bar{\mathbf{v}} \in \mathbb{R}^n$ is formed by applying a linear transformation to the input vector $\bar{\mathbf{p}} \in \mathbb{R}^m$ of projection data. Let $\mathcal{S}^{(t)} : \mathbb{R}^m \rightarrow \mathbb{R}^n$ denote the linear operator that corresponds with t iterations of the SIRT algorithm, starting with $\bar{\mathbf{v}}^{(0)} = \mathbf{0}$.

$$\bar{\mathbf{v}} = \mathcal{S}^{(t)} \bar{\mathbf{p}}, \quad (4)$$

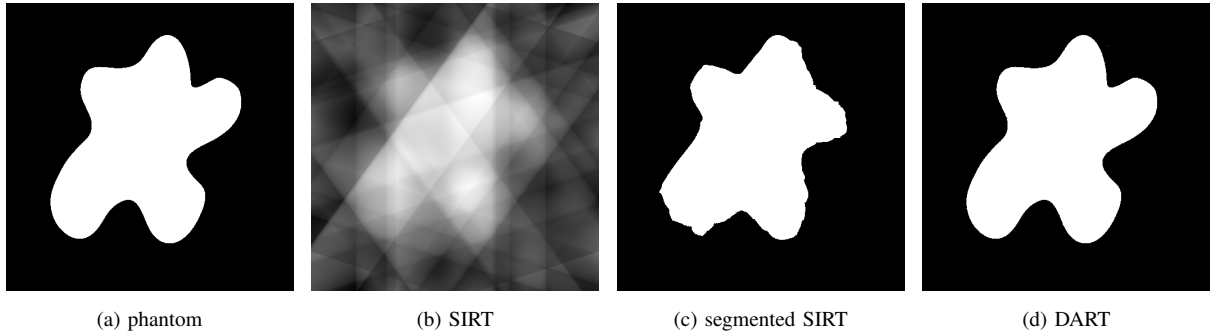


Fig. 3. (a) A binary 512×512 phantom image. (b) SIRT reconstruction from 5 equiangular parallel beam projection directions. (c) Otsu's segmentation of (b). (d) DART reconstruction from 5 equiangular parallel beam projection directions.

The SIRT algorithm can also be performed on a certain subset $A \subset \{1, \dots, n\}$ of the reconstruction grid by removing the columns of \mathbf{W} that are not in A . Consider the case where $A = \{1, \dots, n\} \setminus \{j\}$, with $j \in \{1, \dots, n\}$. Eq. (2) then becomes:

$$\begin{pmatrix} \vdots & & \vdots & & \vdots \\ w_{i,1} & \dots & w_{i,j-1} & w_{i,j+1} & \dots & w_{i,n} \\ \vdots & & \vdots & & \vdots & \end{pmatrix} \begin{pmatrix} v_1 \\ \vdots \\ v_{j-1} \\ v_{j+1} \\ \vdots \\ v_n \end{pmatrix} = \begin{pmatrix} p_1 \\ \vdots \\ p_m \end{pmatrix}. \quad (5)$$

Let $\mathcal{S}_A^{(t)} : \mathbb{R}^m \rightarrow \mathbb{R}^n$ denote the linear operator that corresponds with t iterations of the SIRT algorithm, restricted to a set of pixels $A \subset \{1, \dots, n\}$, starting with $\bar{\mathbf{v}}^{(0)} = \mathbf{0}$.

$$\bar{\mathbf{v}} = \mathcal{S}_A^{(t)} \bar{\mathbf{p}}. \quad (6)$$

Prior to analysis of the reconstructed images, they are often segmented using a simple global thresholding scheme. The segmented image is then computed from the reconstructed image where each pixel is assigned one of the grey levels in $\rho \in \mathbb{R}^l$ according to threshold values $\tau \in \mathbb{R}^{l-1}$. Let l denote the number of unique grey levels. Define the threshold function $\mathcal{C}_{\tau, \rho}(\bar{\mathbf{v}}) : \mathbb{R}^n \rightarrow \{\rho_1, \dots, \rho_l\}^n$ as

$$\mathcal{C}_{\tau, \rho}(\bar{v}_j) = \begin{cases} \rho_1 & \bar{v}_j < \tau_1 \\ \rho_2 & \tau_1 \leq \bar{v}_j < \tau_2 \\ \vdots & \\ \rho_l & \tau_{l-1} \leq \bar{v}_j \end{cases}, \quad j = 1, \dots, n. \quad (7)$$

III. METHODS

Consider the case presented in Fig. 3, where a binary 512×512 phantom image (Fig. 3a) is reconstructed with only 5 projection directions. The reconstruction problem is very ill-posed, leading to multiple solutions that adhere

to the projection data. In that case, the SIRT reconstruction (Fig. 3b) converges to the solution of which its weighted Euclidean distance to the initial image (here a black image) is minimal [10].

To create a segmented image, a global thresholding scheme is typically applied to the reconstructed image. **Otsu's clustering method** [11] is commonly used. However, Otsu's method determines its threshold values solely on the basis of the reconstructed image and thus also on its reconstruction artefacts (shown in Fig. 3c). In [12], an advanced tomographic segmentation technique, called ***Projection Distance Minimization (PDM)*** was proposed. In PDM, thresholds values are selected such that the Euclidean distance between the forward projection of the segmented image and the measured projection data is minimal. This method is further investigated in Section III-A.

Note that in Fig. 3c, most of the segmentation errors occur near the border of the object. This observation lies at the core of the ***Discrete Algebraic Reconstruction Technique (DART)***, an iterative reconstruction technique that combines conventional iterative reconstruction techniques and segmentation into a single algorithm [1]. In each DART iteration, non-boundary pixels are assigned a given grey level in the known set $\rho = (\rho_i) \in \mathbb{R}^l$. These pixels are then kept fixed in the subsequent reconstruction step. This reduces the amount of unknowns in the reconstruction equation Eq. (2) while keeping the amount of detector values stable, thus leading to improved reconstructions. Fig. 3d shows a DART reconstruction of the phantom image in Fig. 3a from only 5 projections. DART is discussed in detail in Section III-B.

Finally, in Section III-C, DART is extended with a novel approach to automatically estimate the set of discrete grey levels.

A. Projection Distance Minimization (PDM)

The optimal tomographic image in which the possible grey levels are restricted to those in the set $\rho \in \mathbb{R}^l$, is the one for which the Euclidean distance between its forward projection and the measured projection data is minimal. Let $s_{opt} \in \{\rho_1, \dots, \rho_l\}^n$ denote this image:

$$s_{opt} = \operatorname{argmin}_{s \in \{\rho_1, \dots, \rho_l\}^n} \|Ws - p\|_2. \quad (8)$$

The search space of the optimization problem in Eq. (8) has a very high dimensionality, making it difficult to locate the optimum. Therefore, segmented images are commonly obtained by application of a global thresholding scheme on a certain, priorly reconstructed image v . The optimization problem of Eq. (8) can then be translated into

$$\tau_{opt}, \rho_{opt} = \operatorname{argmin}_{\tau \in \mathbb{R}^{l-1}, \rho \in \mathbb{R}^l} \|W\mathcal{C}_{\tau, \rho}(v) - p\|_2. \quad (9)$$

The dimension of the search space of the optimization problem in Eq. (9) is only $2l - 1$. To further increase the computational efficiency of the optimization, it can be split into two smaller optimization problems:

- Inner optimization: Given certain threshold values $\bar{\tau}$, determine the optimal grey levels, ρ_{opt} , that minimize Eq. (9):

$$\rho_{opt} = \operatorname{argmin}_{\rho} \|W\mathcal{C}_{\bar{\tau}, \rho_{opt}}(v) - p\|_2. \quad (10)$$

This optimization problem is discussed in Section III-A1.

- Outer optimization: Optimize τ by solving

$$\tau_{opt} = \operatorname{argmin}_{\tau} \|\mathbf{W}\mathcal{C}_{\tau, \rho_{opt}}(\mathbf{v}) - \mathbf{p}\|_2. \quad (11)$$

In each function evaluation, ρ_{opt} is given by the inner optimization. The outer optimization problem is discussed in Section III-A2.

1) *Grey level estimation:* Given an image vector \mathbf{v} and certain threshold values $\bar{\tau}$, for each $t \in \{1, \dots, l\}$, let $\bar{s}_t \in \{0, 1\}^n$ denote the *partition mask* of class t :

$$\bar{s}_{tj} = \begin{cases} 1 & \text{if } \mathcal{C}_{\bar{\tau}, \{1, \dots, l\}}(v_j) = t \\ 0 & \text{otherwise} \end{cases}, \quad j = 1, \dots, n. \quad (12)$$

Let $\mathbf{A} = (a_{it})$ denote an $m \times l$ matrix where column t contains the forward projection of \bar{s}_t . The value a_{it} is defined by the total contribution to ray i of all pixels that belong to partition t .

$$a_{it} = \sum_{j=1}^n w_{ij} \bar{s}_{ti} = \sum_{j: \bar{s}_{ti}=1} w_{ij} \quad (13)$$

For any set of grey levels ρ , the forward projection of $\mathcal{C}_{\bar{\tau}, \rho}(\mathbf{v})$ can then be written as

$$\mathbf{W}\mathcal{C}_{\bar{\tau}, \rho}(\mathbf{v}) = \sum_{t=1}^l \mathbf{W}\bar{s}_t \rho_t = \mathbf{A}\rho. \quad (14)$$

Let \mathbf{a}_j denote the j^{th} row of \mathbf{A} and let $\mathbf{c}_j = -2p_j \mathbf{a}_j$, $\bar{\mathbf{c}} = \sum_{j=1}^m \mathbf{c}_j$, $\mathbf{Q}_j = \mathbf{a}_j \mathbf{a}_j^T$, $\bar{\mathbf{Q}} = \sum_{j=1}^m \mathbf{Q}_j$. The projection difference then becomes:

$$\|\mathbf{W}\mathcal{C}_{\bar{\tau}, \rho}(\mathbf{v}) - \mathbf{p}\|_2 = \|\mathbf{A}\rho - \mathbf{p}\|_2 \quad (15)$$

$$= \sum_{j=1}^m (\mathbf{a}_j^T \rho - p_j)^2 \quad (16)$$

$$= \sum_{j=1}^m (\rho^T \mathbf{Q}_j \rho - \mathbf{c}_j^T \rho + p_j^2) \quad (17)$$

$$= \rho^T \bar{\mathbf{Q}} \rho - \bar{\mathbf{c}}^T \rho + |\mathbf{p}|^2 \quad (18)$$

Given that the projection difference can not be negative, the optimal grey levels, ρ , can be computed by setting the derivatives of Eq.(18) with respect to ρ_1, \dots, ρ_l to zero, obtaining the easy to solve system:

$$2\bar{\mathbf{Q}}\rho_{opt} = -\bar{\mathbf{c}}. \quad (19)$$

2) *Threshold value estimation:* To optimize τ , Eq.(11) must be solved. Each evaluation in the search space requires the computation of ρ_{opt} . Note that Eq.(11) is not differentiable. In [12], a strategy was proposed to efficiently optimize Eq.(11). It made use of the fact that, if the threshold values are changed only by a small amount, only a few pixels would fall into a different partition. The matrices $\bar{\mathbf{c}}$ and $\bar{\mathbf{Q}}$ could therefore be updated very efficiently. However, such an approach is not optimally suited for optimization on modern GPU hardware and its overall runtime depends greatly on the initial estimate. We have found that it is typically more computationally efficient to compute GPU-accelerated forward projections of all pixels at each function evaluation. Experimental

findings have shown that the Nelder-Mead simplex search [7] offers accurate results with a sufficiently fast convergence rate.

B. Discrete Algebraic Reconstruction Technique (DART)

Here, a concise summary of the iterative DART algorithm is given. Initially, an approximate reconstruction image, $\mathbf{v}^{(0)}$, is computed using SIRT with a certain number of iterations, t_0 :

$$\mathbf{v}^{(0)} = \mathcal{S}^{(t_0)} \mathbf{p}. \quad (20)$$

Next, DART follows an iterative scheme with the following steps. Put $k = 0$, the iteration number of DART.

- 1) The current reconstructed image, $\mathbf{v}^{(k)}$, is segmented to obtain an image that contains only grey levels from the set $\rho \in \mathbb{R}^l$. A simple global thresholding scheme with threshold values $\tau \in \mathbb{R}^{l-1}$ is used. Let $\mathbf{s}^{(k)} \in \{\rho_1, \dots, \rho_l\}^n$ denote that segmented image:

$$\mathbf{s}^{(k)} = \mathcal{C}_{\tau, \rho}(\mathbf{v}^{(k)}). \quad (21)$$

- 2) The set $U^{(k)} \subset \{1, \dots, n\}$ of *pixels to be updated* is determined. This set contains pixels that are likely to be misclassified in the current segmented image. The pixels in the complementary set of *fixed pixels* $F^{(k)} = \{1, \dots, n\} \setminus U^{(k)}$ are those that will be removed from the reconstruction equation. $U^{(k)}$ contains two types of pixels:
 - As demonstrated in Fig. 3c, most errors occur near the edges of the object. All boundary pixels of the current segmented image are thus added to $U^{(k)}$. A pixel is considered to be a boundary pixel if its value is different from at least one of its neighbouring pixels:

$$U^{(k)} = \left\{ j : \exists h \in N(j) \text{ such that } s_j^{(k)} \neq s_h^{(k)} \right\}. \quad (22)$$

In Eq. (22), $N(j) \subset \{1, \dots, n\}$ denotes a certain neighbourhood window of pixel j . In [13], a variation of DART, called *Adaptive DART (ADART)*, was introduced. In ADART, the required number of pixels from $h \in N(j)$ for which $s_j^{(k)} \neq s_h^{(k)}$ is increased each time a certain convergence criterion is met. This can lead to improved reconstruction quality.

- Each non-boundary pixel is added to $U^{(k)}$ with a certain probability $0 \leq r \leq 1$. This increases the accuracy of DART reconstruction in case of noisy projection data.
- 3) To reduce the set of unknowns in Eq. (2) to those in the set of free pixels, the forward projection of the non-free pixels must first be subtracted from the measured projection data. Let $\mathbf{f}^{(k)} \in \mathbb{R}^n$ denote the current segmented image in which all free pixels are set to zero, i.e.

$$f_j^{(k)} = \begin{cases} s_j^{(k)} & j \notin U^{(k)} \\ 0 & j \in U^{(k)} \end{cases}. \quad (23)$$

The *residual sinogram*, $\mathbf{r}^{(k)} \in \mathbb{R}^m$, is then given by

$$\mathbf{r}^{(k)} = \mathbf{p} - \mathbf{W} \mathbf{f}^{(k)}. \quad (24)$$

- 4) The current reconstructed image is then updated by the reconstruction of the residual sinogram, restricted to the set of free pixels:

$$\mathbf{v}^{(k+1)} = \mathbf{f}^{(k)} + \mathcal{S}_{U^{(k)}}^{(t)} \mathbf{r}^{(k)}. \quad (25)$$

In Eq. (25), t denotes the number of SIRT iterations that are performed to reconstruct the residual sinogram. If certain pixels are misclassified in step 1, the residual sinogram is inconsistent. In that case, there does not exist an exact solution to Eq. (25), leading to erroneous values in the updated reconstruction. To counter this, a Gaussian smoothing filter is applied to $\mathbf{v}^{(k+1)}$ as a means of regularization.

- 5) Increase k by 1 and return to step 1 until some termination criterion has been reached.

C. PDM-DART

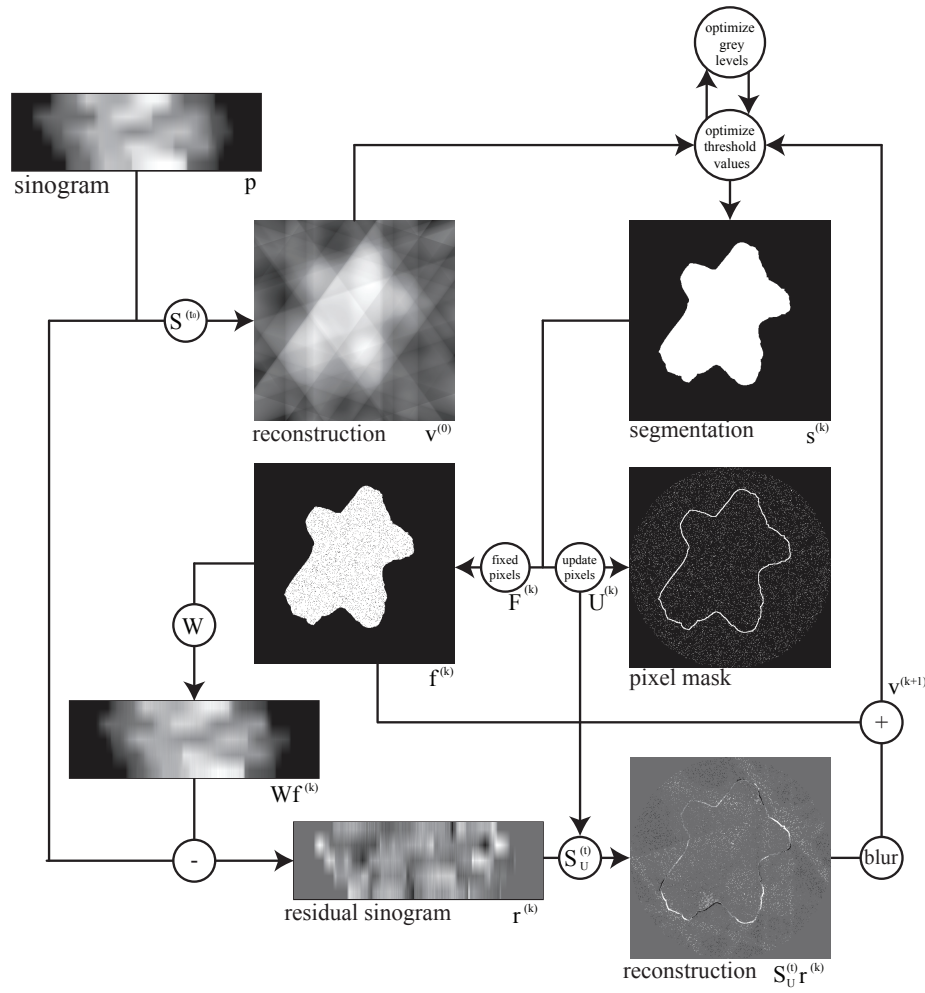


Fig. 4. Schematic overview of Projection Distance Minimization Discrete Algebraic Reconstruction Technique (PDM-DART).

In step 1 of each DART iteration a segmented image is computed from $\mathbf{v}^{(k)}$ using a global thresholding scheme with fixed, priorly specified, grey levels ρ and threshold values τ . Here, it is proposed to apply the PDM method,

```

 $v = \mathcal{S}^{(t_0)} p;$ 
 $\tau = \text{initial threshold estimate};$ 
while stop criterion is not met
   $[\tau, \rho] = \text{estimate\_segmentation\_parameters}(v, \tau);$ 
   $s = \mathcal{C}_{\tau, \rho}(v);$ 
   $U = \{\};$ 
  for  $j = 1:n$ 
    if  $(\exists h \in N(j) : s_j \neq s_h) \quad || \quad \text{rand}() < r$ 
       $f_j = 0;$ 
       $U = U \cup j;$ 
    else
       $f_j = s_j;$ 
    end
  end
   $r = p - Wf;$ 
   $v = f + \mathcal{S}_U^{(t)} r;$ 
   $v = v * \text{Gaussian smoothing filter} ;$ 
end

function  $[\tau_{opt}, \rho_{opt}] = \text{estimate\_segmentation\_parameters}(v, \tau_{init})$ 
   $[\tau_{opt}, \rho_{opt}] = \text{simplex search of } @\text{compute\_projection\_distance} \text{ with } \tau_{init} \text{ as initial estimate} ;$ 
end

function  $[\text{projection\_difference}, \rho_{opt}] = \text{compute\_projection\_distance}(\tau)$ 
  compute  $A$ ;
  compute  $\bar{Q}$  and  $\bar{c}$ ;
   $\rho_{opt} = \text{solution of } 2\bar{Q}\rho = -\bar{c} \text{ w.r.t } \rho;$ 
   $\text{projection\_difference} = \|W\mathcal{C}_{\tau, \rho_{opt}}(v) - p\|_2;$ 
end

```

Fig. 5. Pseudo code for the Projection Distance Minimization Discrete Algebraic Reconstruction Technique (PDM-DART).

as discussed in Section III-A, to automatically estimate the segmentation parameters *within* each DART iteration. The novel method is called *Projection Distance Minimization DART (PDM-DART)*. PDM-DART is schematically visualised in Fig. 4. In Fig. 5, simplified pseudo code is listed.

For low values of k , intermediate reconstructions, $v^{(k)}$, are typically very inaccurate. The application of PDM is then likely to result in inaccurate segmentation parameters. However, as the experimental results in Section IV demonstrate, even in that case the next intermediate reconstruction, $v^{(k+1)}$, is very likely to improve. This will then make the subsequently optimised segmentation parameters more accurate, ultimately converging to high quality parameter estimations and reconstructed images.

Note that classical threshold selection techniques, such as Otsu's clustering methods [11] or k-means clustering,

are not suited for use within DART. Incorrect grey levels of an intermediate segmentation will negatively affect the selection of new segmentation parameters in the subsequent iteration. In PDM, however, the optimal grey levels are based on the measured projection data, not on the values obtained in the reconstructions.

The segmentation parameter estimation process does present an increased computational cost to each iteration of the DART algorithm. To reduce this cost, one can opt to perform this optimization only once every few iterations. The optimised segmentation parameters are then stored and reused until the next optimization takes place.

IV. EXPERIMENTS

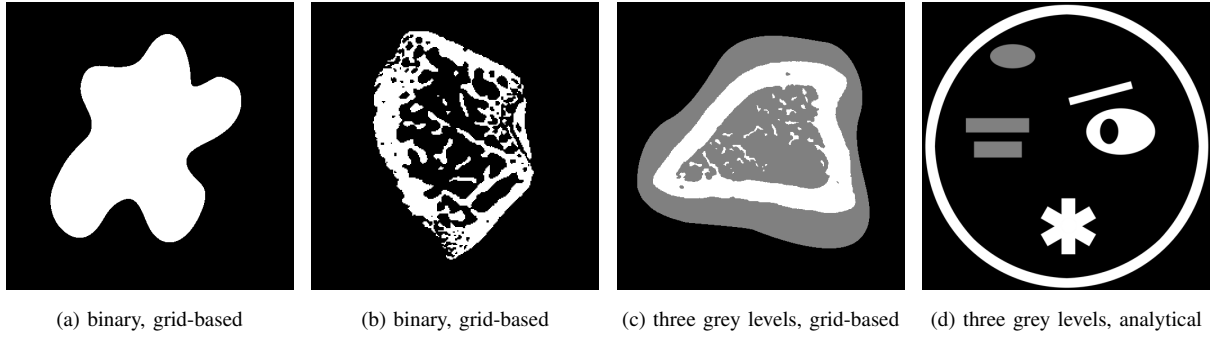


Fig. 6. Simulated phantoms that are used to validate PDM-DART.

In this section, a series of experiments are described that were carried out to evaluate PDM-DART. Both simulation data and experimental μ CT data are included.

For all simulation experiments, four phantom images were considered (Fig. 6). Whereas Fig. 6a and Fig. 6b are binary, Fig. 6c and Fig. 6d contain three grey levels. Fig. 6a-c were defined on a 512×512 grid while Fig. 6d, and its projection data, were analytically defined. All reconstructions were performed on a 512×512 grid. Only parallel beam projection geometries with equiangular projection angles have been considered. However, the proposed method can easily be applied on other projection geometries as well. *which other geometries ?*

To validate the accuracy of the segmented images, the *relative Number of Misclassified Pixels (rNMP)* was computed. This is the total number of erroneously classified pixels with respect to the phantom, divided by the total number of non-zero pixels in the phantom image.

All experiments were performed on a single-core 2.4GHz system with 8GB memory. All tomographic operations, such as DART, SIRT and the forward projection, were accelerated with NVIDIA CUDA and were run on an NVIDIA GeForce GTX285.

A. Comparison of different estimation methods

In a first set of experiments, projection data was simulated of all phantom images depicted in Fig. 6. The number of projection directions was varied. The following segmentation parameter estimation methods were applied.

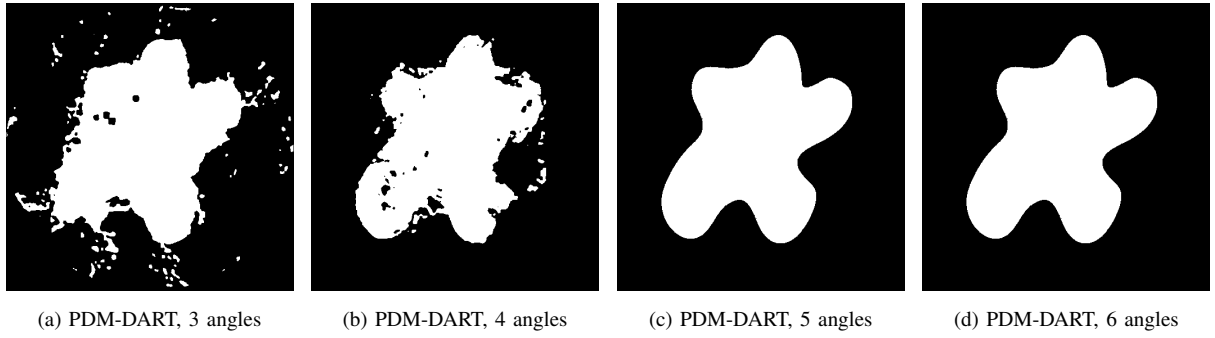


Fig. 7. PDM-DART reconstructions of Fig. 6a with an increasing number of projection directions.

angles	search	manual	DGLS	simplex	PDM-DART
3	0.0947	0.1280	0.2068	0.1208	0.2117
4	0.0575	0.0798	0.1019	0.0911	0.1057
5	0.0007	0.0009	0.0022	0.0014	0.0008
6	0.0006	0.0009	0.0017	0.0009	0.0008
7	0.0004	0.0004	0.0009	0.0012	0.0004
8	0.0003	0.0004	0.0004	0.0003	0.0003
9	0.0002	0.0002	0.0003	0.0003	0.0002
10	0.0001	0.0001	0.0001	0.0001	0.0001

Fig. 8. This table lists, for phantom image Fig. 6a, the reconstruction accuracy in terms of rNMP for a variety of different segmentation parameter estimation methods.

phantom	rNMP goal	search	manual	DGLS	simplex	PDM-DART
Fig. 6a	0.001	5	5	5	5	5
Fig. 6b	0.050	38	39	44	40	43
Fig. 6c	0.010	28	33	36	32	33
Fig. 6d	0.100	16	21	34	17	16

Fig. 9. This table lists, for each image of Fig. 6, the lowest number of projection directions with which it is possible to reach a certain rNMP goal.

- **Exhaustive parameter search:** The parameters resulting in the most accurate reconstructions were found by performing an exhaustive search. This method can only be applied for simulation experiments.
- **Manual selection** (Fig. 2a): The grey levels were measured in the phantom images. The threshold values were set in the middle of each pair of consecutive grey levels.
- **DGLS** (Fig. 2b): The user-selected regions were manually chosen based on an initial SIRT reconstruction. The threshold values were again set in the middle of each pair of consecutive grey levels. A positivity constraint was included in the DGLS optimization process, as described in [5], as this was observed to result in more

accurate estimations.

- **Optimization** (Fig. 2c). The Nelder-Mead simplex search optimization strategy was performed on Eq. (9) to estimate all grey levels and threshold values.
- **PDM-DART** (Fig. 2d). With PDM-DART, all grey levels and threshold values were estimated in each iteration of DART.

In Fig. 7a-d, PDM-DART reconstructions are shown of phantom image Fig. 6a, for an increasing number of projection directions. The rNMP values of these reconstructions, are listed in Fig. 8 for all previously mentioned estimation methods. Both manual estimation and PDM-DART provided the best approximation of the optimal values discovered by the exhaustive parameter search. Simplex search was slightly less accurate. This is likely due to various local optima in the search space. The DGLS approach was also slightly less accurate, especially for very low angle counts.

It can be clearly noted that, for phantom image Fig. 6a, there exists a certain lower bound to the number of projection angles that is required to create highly accurate reconstructions (5 in this example). For all phantom images and estimation methods, it was determined how many projection directions were needed in order to reach a certain level of accuracy (in rNMP values). These results are shown in Fig. 9. Overall, PDM-DART did not require substantially more projection directions to reach a certain accuracy than with the optimal segmentation parameters.

The same experiments were also performed with ADART [13] instead of DART, achieving similar results.

B. PDM-DART convergence

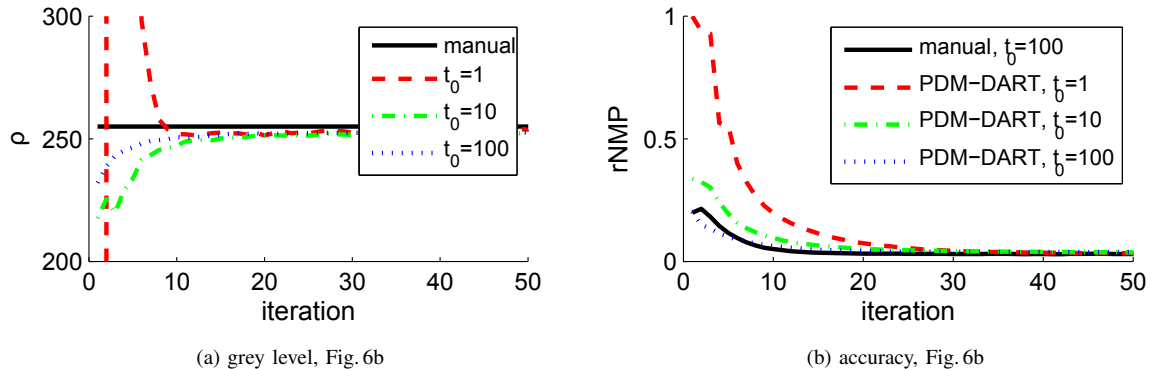


Fig. 10. To study how PDM-DART performs when initial reconstructions do not allow for accurate tomographic segmentation, the algorithm was run with different values for t_0 , the number of SIRT iterations to create $\mathbf{v}^{(0)}$. (a) The estimated grey level of the foreground of phantom image Fig. 6b as a function of the iteration number. (b) The corresponding accuracy in terms of rNMP.

It may be expected that, if the parameter estimation in PDM-DART is very inaccurate in one iteration, it can still be improved in subsequent iterations.

To investigate the dependence of inaccurate parameter estimation in one iteration on the eventual result, projection data of each phantom image was generated for 30 projections to which Poisson noise was applied. The intensity

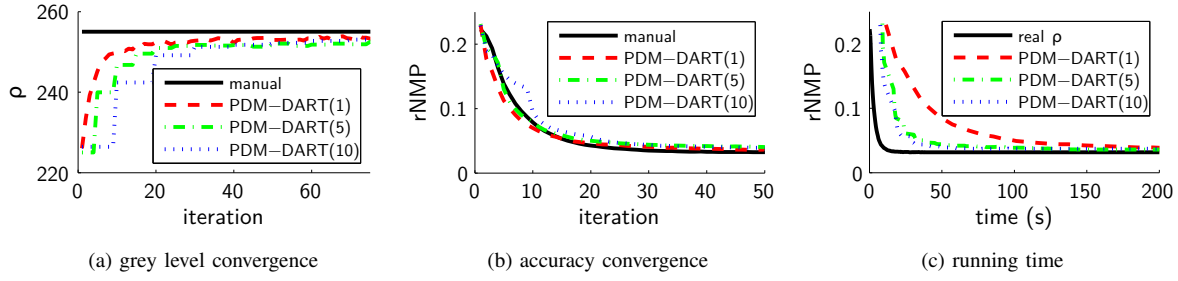


Fig. 11. (a) The chosen grey level of the foreground of Fig. 6b as a function of the iteration number. (b) The corresponding accuracy in terms of rNMP. (c) The total running time of the algorithm as a function of the running time.

of this noise is defined by the *incident beam intensity*, I_0 , i.e. the photon count in the incident X-ray beam. Here, I_0 was 50000. PDM-DART reconstructions were performed using different values for t_0 , the number of SIRT iterations that were performed to compute $v^{(0)}$. For low values of t_0 , the intermediate reconstructions in the first few iterations are typically severely inaccurate, leading to highly inaccurate segmentation parameters.

In Fig. 10a, the grey level estimation of the foreground of phantom image Fig. 6b is visualised as a function of the iteration number. The correct grey level, 255, is also visualised. It can be seen that, even if the estimated grey level was initially inaccurate, after a few iterations the correct grey level was still adequately approximated. The accuracy of the corresponding reconstructed images is plotted in Fig. 10b. Even for very low values of t_0 , the accuracy of the images was comparable to those computed with a manual approach. However, for low values of t_0 , PDM-DART did require more computationally demanding iterations.

C. Possible speedup of PDM-DART

In Section III-A2, it was suggested that the additional computational load of PDM-DART over regular DART can be limited by performing the parameter optimization only once per block of iterations. This was experimentally validated on all phantom images, with a parallel beam projection geometry with 30 projection angles and with $I_0 = 50000$.

In Fig. 11a and Fig. 11b, it can be seen that for Fig. 6b, even if the optimization was performed only once every ten iterations, accurate parameter estimation and reconstruction were still obtained. While the convergence speed towards these results was slower and more iterations were thus demanded to reach a certain level of accuracy, the overall runtime was still substantially decreased. This can be seen in Fig. 11c.

D. Limited angles and noisy data

Next, the effect of noise on the projection data was studied by performing experiments on all phantom images of Fig. 6, using all parameter estimation methods visualised in Fig. 2. To reduce computation time for phantom images Fig. 6c and Fig. 6d, only the grey levels were estimated in the simplex search approach. Threshold values were then always put in the middle of two grey levels. For all PDM-DART experiments, parameter estimation was performed only once every 10 iterations.

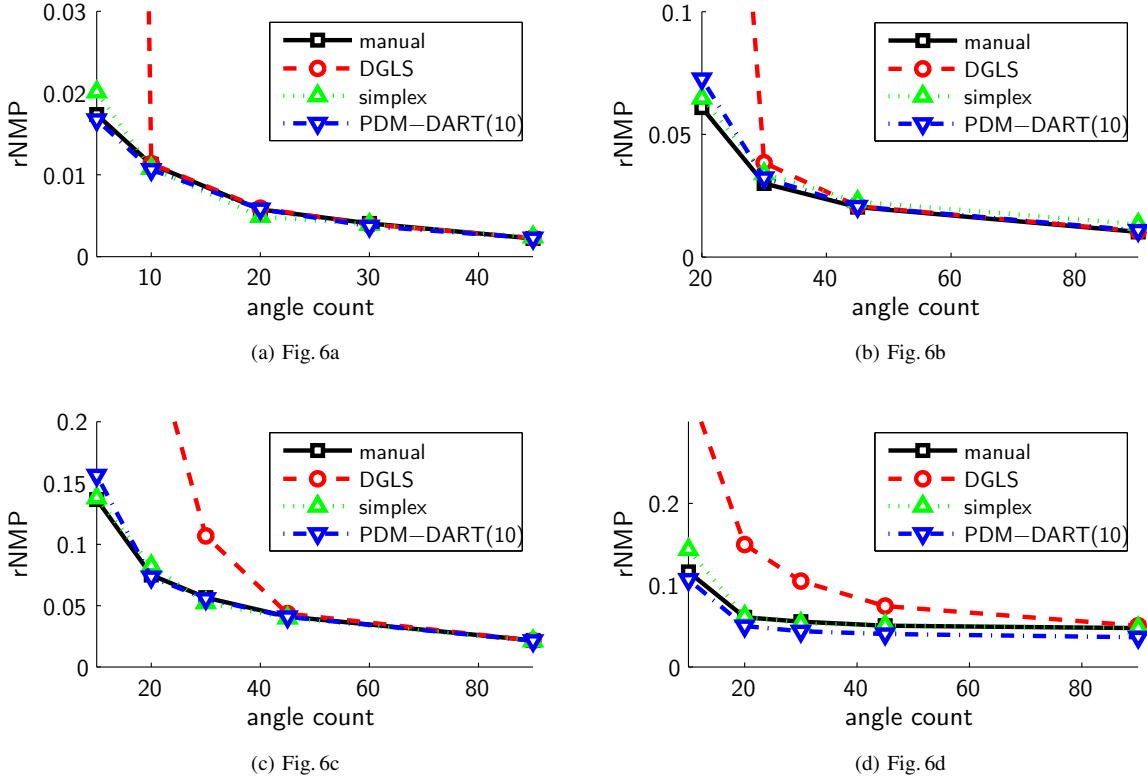


Fig. 12. The rNMP values for reconstructed images of each phantom image of Fig. 6 as a function of the number of projection angles, for four different parameter estimation methods. The projection data was generated for a parallel beam projection geometry on which Poisson noise with intensity $I_0 = 50000$ was applied.

In Fig. 12, the rNMP values of the different parameter estimation schemes are plotted as a function of the number of projection angles used for the reconstruction. In these experiments, the incident beam intensity I_0 was set to 50000. Even in the presence of noise, the PDM-DART algorithm did not require substantially more projection directions than the manual approach with optimal grey levels. DGLS, however, generally required more projection directions to provide accurate grey level estimations. This was especially true for objects for which it was not possible to select large homogeneous parts in an initial reconstruction.

In Fig. 13, the rNMP values are plotted as a function of the beam intensity, using 45 projection angles. There were 45 angles in the projection geometry. The achievable accuracy clearly decreased as the noise level increased. If the level of the noise was very high, the simplex search method was often not able to find the global optimum.

In Fig. 14, the runtimes of the various estimation methods are plotted for each phantom image of Fig. 6 (with $I_0 = 50000$ and 45 projection angles). Given that these runtimes are dependent on the implementation, they only offer a rough overview of the computational efficiency. The fastest reconstructions occurred when the grey levels and threshold values were manually supplied and no further estimation was required. The addition of the DGLS method as an extra pre-processing step slightly increased the reconstruction time. Note, however, that these timings

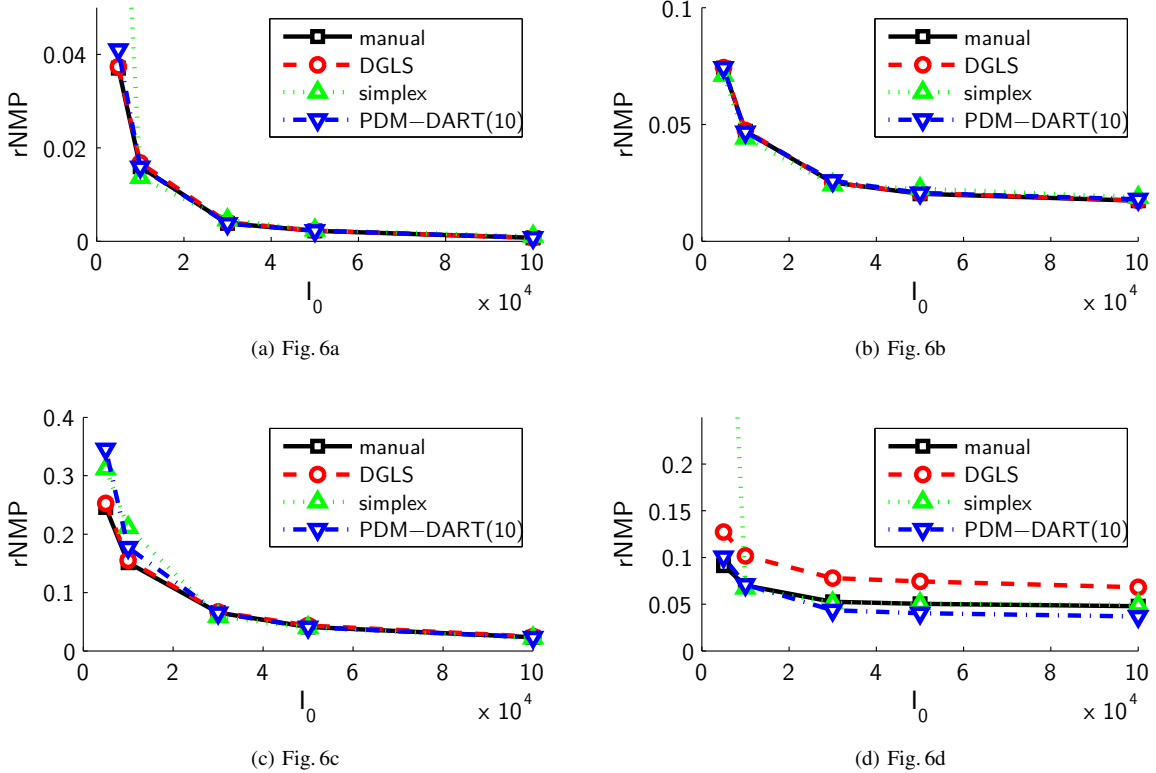


Fig. 13. The rNMP values for reconstructed images of each phantom image of Fig. 6 as a function of the intensity of the applied Poisson noise, for four different parameter estimation methods. The projection data was generated for a parallel beam projection geometry with 45 equiangular projection angles.

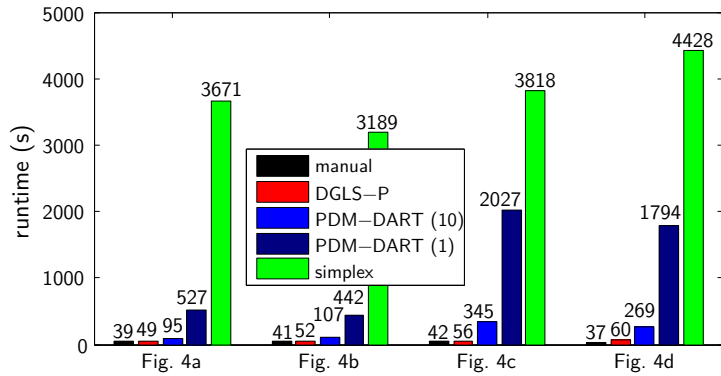


Fig. 14. The runtimes of each estimation method for each of the phantom images of Fig. 6 with simulated parallel beam projection data with 45 angles and $I_0 = 50000$.

do not take into account the extra time that it took to select the homogeneous part. The PDM-DART scheme required more computation time than DGLS, especially for high-dimensional optimization problems (e.g. Fig. 6c

and Fig. 6d). However, the runtime was reduced by excluding the estimation of the segmentation parameters. The simplex search scheme required by far the most computation time.

E. Experimental data

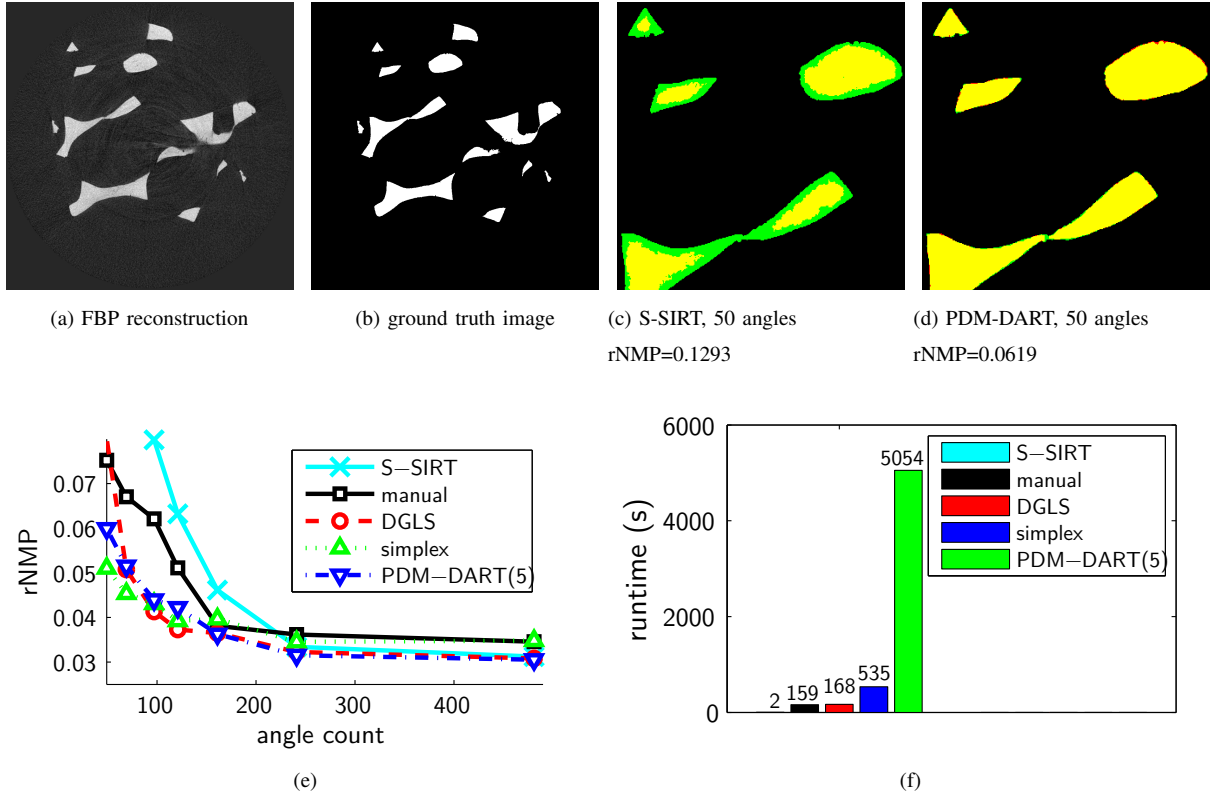


Fig. 15. Results of the experimental μ CT dataset of an aluminium foam. (a) FBP reconstruction with 481 projection angles. (b) The segmentation of (a) is used as the ground truth image. (c,d) Part of PDM-DART reconstructions with 481 and 50 projection angles. The ground truth image is displayed in red and the reconstructions in green. Where both images overlap, i.e. where the segmentation is correct, the corresponding pixel is yellow. (e) The rNMP w.r.t to (b) of various estimation methods, in function of the number of projection directions.

The proposed method was also applied on experimental μ CT data. Fig. 15a shows an FBP reconstruction of a slice through an aluminium foam, which was recorded with a SkyScan 1172 μ CT scanner with 481 equiangular projection angles in the interval $[0, \pi]$. The detector resolution was $9.7\mu\text{m}$. Prior to reconstruction, the data was corrected for ring artefacts and beam hardening with the standard SkyScan NRecon software package.

In Fig. 15b, the segmentation of Fig. 15a, performed with Otsu's clustering method [11], is shown. This image was used as the ground truth. Next, the number of projection angles in the sinogram was gradually reduced and reconstructions were performed with five different techniques: (1) S-SIRT (a SIRT reconstruction segmented using Otsu's method); (2) a manual approach in which the median value of a user-selected part was used to estimate the

grey levels; (3) the DGLS approach; (4) the simplex search method; and (5) PDM-DART. Fig. 15c and Fig. 15d show the S-SIRT and PDM-DART reconstructions from only 50 projection images respectively. In Fig. 15e, all computed rNMP values are plotted in function of the angle count. In Fig. 15f, runtimes are shown. Note that, only for a very small number of projections, the slow simplex search method slightly outperforms the PDM-DART approach, which, in turn, slightly outperforms the fast DGLS approach.

V. DISCUSSION

In the previous section, a series of experiments was described in which the novel PDM-DART approach was compared to other parameter estimation techniques. Each strategy has upsides as well as downsides:

- In simulation experiments, **manual estimation** (Fig. 2a) generally provides the highest quality reconstructed images with the least amount of time. However, this method is often not feasible in practical applications as various reconstruction artefacts can prevent accurate estimation.
- The **DGLS** technique (Fig. 2b) can generate accurate grey level estimations prior to the DART reconstruction and does not present a significant computational overhead. However, it cannot be used to optimally select the threshold values and it can only be applied if the user-based selection of homogeneous areas is easy. It also tends to be inaccurate if the number of projection angles is very low. It is only *semi-automatic*.
- Optimization with the commonly used Nelder-Mead **simplex search strategy** (Fig. 2c) can approximate all optimal segmentation parameters. Given that DART is a non-deterministic algorithm, a typical search space contains many local optima. However, experiments have shown that very accurate estimations can still be made. Furthermore, the method is *fully automatic* and can also be used to optimize other algorithm parameters such as the number of additional random pixels in $U^{(k)}$ in step 2 of each DART iteration or the intensity of the smoothing filter in step 4 of each DART iteration. Estimation with this method is computationally intensive.
- The *fully automatic* **PDM-DART** (Fig. 2d) generally results in accurate reconstructions even in cases where the DGLS method typically fails. While its computational overhead is substantially lower than the simplex estimation scheme, it is drastically larger than DGLS or manual estimation, especially for high dimensional estimation problems, i.e. if there are many unique grey levels present in the image. This dimensionality can be reduced by removing the grey level of the background, which should always be 0, or by excluding the estimation of the threshold values, fixing them at the middle of two grey levels. With a minimal loss of accuracy, a large speedup can also be achieved if the estimation of segmentation parameters is performed only once per a certain number of DART iterations.

VI. CONCLUSIONS

In this work, a novel estimation method for use within DART was proposed. PDM-DART combines discrete reconstruction with estimation of segmentation parameters. In contrast to classical DART, where these parameters remain fixed throughout the entire reconstruction process, PDM-DART adaptively selects the optimal segmentation parameters *within* each DART iteration.

Experiments have been performed on a range of different simulation images as well as on experiment μ CT data. They have confirmed that with the PDM-DART approach, high quality reconstructions can be made even for a low number of projection angles. Furthermore, it was demonstrated that the use of PDM-DART does not require more projection directions than other estimation methods. This paves the way for fully automatic discrete tomography in a wide range of applications, (e.g. materials science, biomedical research, ...). Thus far, this was a highly labour intensive procedure.

REFERENCES

- [1] K. J. Batenburg and J. Sijbers, "DART: A practical reconstruction algorithm for discrete tomography," *IEEE Transactions on Image Processing*, vol. 20, no. 9, pp. 2542–2553, 2011.
- [2] K. J. Batenburg, S. Bals, J. Sijbers, C. Kübel, P. A. Midgley, J. C. Hernandez, U. Kaiser, E. R. Encina, E. A. Coronado, and G. Van Tendeloo, "3D imaging of nanomaterials by discrete tomography," *Ultramicroscopy*, vol. 109, no. 6, pp. 730–740, 2009.
- [3] S. Bals, K. J. Batenburg, D. Liang, O. Lebedev, G. Van Tendeloo, A. Aerts, J. A. Martens, and C. E. Kirschhock, "Quantitative three-dimensional modeling of zeotile through discrete electron tomography," *Journal of the American Chemical Society*, vol. 131, no. 13, pp. 4769–4773, 2009.
- [4] K. J. Batenburg, J. Sijbers, H. F. Poulsen, and E. Knudsen, "DART: a robust algorithm for fast reconstruction of three-dimensional grain maps," *Journal of Applied Crystallography*, vol. 43, no. 6, pp. 1464–1473, 2010.
- [5] K. J. Batenburg, W. van Aarle, and J. Sijbers, "A semi-automatic algorithm for grey level estimation in tomography," *Pattern Recognition Letters*, vol. 32, no. 9, pp. 1395–1405, 2011.
- [6] W. van Aarle, K. Crombecq, I. Couckuyt, K. J. Batenburg, and J. Sijbers, "Efficient parameter estimation for discrete tomography using adaptive modeling," in *Fully Three-Dimensional Image Reconstruction in Radiology and Nuclear Medicine*, July 2011, pp. 229–232.
- [7] J. C. Lagarias, J. A. Reeds, M. H. Wright, and P. E. Wright, "Convergence properties of the nelder-mead simplex method in low dimensions," *SIAM Journal of Optimization*, vol. 9, no. 1, pp. 112–147, 1998.
- [8] D. Gorissen, K. Crombecq, I. Couckuyt, T. Dhaene, and P. Demeester, "A surrogate modeling and adaptive sampling toolbox for computer based design," *Journal of Machine Learning Research*, vol. 11, pp. 2051–2055, 2010.
- [9] K. J. Batenburg and J. Sijbers, "Optimal threshold selection for tomogram segmentation by projection distance minimization," *IEEE Transactions on Medical Imaging*, vol. 28, no. 5, pp. 676–686, 2009.
- [10] J. Gregor and T. Benson, "Computational analysis and improvement of SIRT," *IEEE Transactions on Medical Imaging*, vol. 27, no. 7, pp. 918–924, 2008.
- [11] N. Otsu, "A threshold selection method from gray level histograms," *IEEE Transactions on Systems, Man, and Cybernetics*, vol. 9, no. 1, pp. 62–66, March 1979.
- [12] K. J. Batenburg and J. Sijbers, "Adaptive thresholding of tomograms by projection distance minimization," *Pattern Recognition*, vol. 42, no. 10, pp. 2297–2305, 2009.
- [13] F. J. Maestre-Deusto, G. Scavello, J. Pizarro, and P. L. Galindo, "ADART: An adaptive algebraic reconstruction algorithm for discrete tomography," *IEEE Transactions on Image Processing*, vol. 20, no. 8, pp. 2146–2152, 2011.